Interplay between local structure and magnetic properties of graded exchange-coupled Co@FePt nanocomposite films

Charles Paleo,[1,*] Véronique Dupuis,[1] Fabrice Wilhelm,[2] Andrei Rogalev,[2] Olivier Proux,[3] Olivier Boisron,[1] Isabelle Kieffer,[3] Thierry Epicier,[4] Matthieu Bugnet,[4] and Damien Le Roy[1]

[1]*Institut Lumière Matière, Université Claude Bernard Lyon 1, CNRS, Villeurbanne F-69622, France*

[2]*The European Synchrotron Radiation Facility (ESRF), 38000 Grenoble, France*

[3]*Observatoire des Sciences de l'Univers de Grenoble, Université Grenoble Alpes, CNRS, 38041 Grenoble, France*

[4]*Université de Lyon, INSA-Lyon, Université Claude Bernard Lyon 1, MATEIS UMR CNRS 5510, Villeurbanne F-69621, France*

(Received 16 September 2020; revised 13 November 2020; accepted 23 November 2020; published 10 December 2020)

Hard magnetic nanocomposites are attractive materials for integration in various microsystems and for building of next-generation permanent magnets. However, exploiting their full potential requires control of their microstructure at the nanometer scale. Studying these materials in model systems synthesized by nanofabrication routes provides interesting insights into the interplay between the microstructure and the magnetic performances. Here, by using a combination of mass-selected low-energy cluster beam deposition and electron-beam evaporation, we prepare nanocomposite films where Co nanoinclusions are integrated in a hard magnetic FePt matrix. Local atomic structures and element-selective magnetic properties of such nanocomposites have been thoroughly investigated using polarization-dependent hard x-ray absorption spectroscopies. These results demonstrate that magnetically soft inclusions are stabilized at room temperature, emphasizing the role of interdiffusion in the preparation of nanocomposites.

DOI: 10.1103/PhysRevB.102.224409

I. INTRODUCTION

Hard magnetic materials with high magnetization are attracting a lot of attention for various applications, from spintronics [1] to magnetic recording media [2,3] or in bulk permanent magnets for energy conversion technologies [4]. The figure of merit of a permanent magnet is the energy product $(\mathrm{BH})_{\max} \leqslant \frac{1}{4}\mu_0 M_s^2$. The limit is attained for an ideal microstructure and a uniaxial texture, which is nearly achieved in NdFeB sintered and oriented magnets. With an outstanding combination of a relatively large magnetization $\mu_0 M_s$ of 1.61 T and a large magnetocrystalline anisotropy leading term K_1 of 4.3 MJ $\cdot$ m^{-3}, they have led the performances of permanent magnets for about 30 years, approaching the $(\mathrm{BH})_{\max}$ theoretical limit of 516 kJ $\cdot$ m^{-3} for these nonnanostructured elements [4]. Designing a hard magnetic material with a magnetization $\mu_0 M_s$ higher than 1.61 T is a necessary—although not sufficient—condition to surpass the performances of today's best rare earth (RE) magnets. Fe-Co alloys could be among the most attractive candidates for permanent magnets, with $\mu_0 M_s \geqslant 1.81$ T for pure Co and up to $\mu_0 M_s = 2.45$ T for $Fe_{65}Co_{35}$. In the latter case, it could push the limit of reachable $(\mathrm{BH})_{\max}$ up to nearly 1.2 MJ $\cdot$ m^{-3} if a square magnetization loop with a coercive field in excess of 1.2 T could be achieved ($\mu_0 H_c \geqslant \frac{\mu_0 M_s}{2}$). However, this relies on our ability to significantly increase the relatively low magnetocrystalline anisotropy ($K_1 \leqslant 20$ kJ $\cdot$ m^{-3}) [5], so far predicted but not fully achieved experimentally [6], even though promising results have recently been reported [7].

In addition to these challenges, the risks associated with the sourcing and the fluctuating cost of RE metals due to geostrategic availability and the pollution during extraction of the raw elements and recycling of the used materials are driving the need to reduce the dependency on REs in high-performance permanent magnets [8–10].

An elegant approach to designing a magnet with a high value of the energy product was proposed by Kneller and Harwig, which consists of the fabrication of nanocomposite (NC) materials combining a hard magnetic phase exchange coupled to a strongly magnetic soft phase [11]. The beneficial effect of this approach was initially demonstrated in 1989 by Coehoorn on $Nd_2Fe_{14}B$-Fe_3B ribbons [12]. This finding stimulated further investigations, including theoretical and modeling studies to optimize the NC structure [11,13]. In order to develop new magnets with unprecedented performances, the volume fraction of the hard magnetic phase should be limited to the minimum needed to fulfill the coercive field criterion [13] $\mu_0 M_s/2$ in an ideal uniaxial anistropic case, further extended to realistic cases by Skomski *et al.* [14]. Under the assumptions of zero magnetic anisotropy in the softer phase and a sharp interface between soft and hard magnetic phases, the maximum size of the soft-phase regions is twice the size of the domain wall width of the hard phase. Therefore, to exploit the full potential of nanocomposite magnets, one needs to control their microstructure at the nanometer scale, including the size of the soft inclusions, their concentration, and the roughness of the interface between the hard and the soft phases. In this context, NC films made from nanofabrication routes are

*charles.paleo@univ-lyon1.fr

foreseen to provide interesting insights in view of guiding the synthesis of bulk systems [14–16].

In this work, we investigate the principle of thin-film NC magnets of Co nanometer-sized grains embedded in a hard FePt matrix (called Co@FePt). The fine microstructure analysis requires techniques allowing the chemical distinction of Fe and Co at the nanometric scale. The chemically ordered $L1_0$-FePt phase presents a magnetocrystalline anisotropy K_1 of 6.6 MJ $\cdot$ m^{-3} and a magnetization of $\mu_0 M_s = 1.43$ T [a maximum $(BH)_{max}$ of 407 kJ $\cdot$ m^{-3}], slightly inferior to that of NdFeB [5]. Besides, the use of expensive elements like Pt for bulk magnets is excluded. However, when it comes to microtechnologies where the fabrication costs generally dominate over the raw material costs, FePt films are of great interest. Indeed, they offer higher resistance against corrosion, compared to RE-based films, which makes them more compatible with standard microfabrication processes. NC films of Co_{50}@$(FePt)_{50}$ would potentially exhibit a 28% higher $(BH)_{max}$ than $L1_0$-FePt alone.

II. METHODS

A. Sample preparation

These Co@FePt transition-metal-based nanocomposites are made from Co soft clusters embedded in an $L1_0$-FePt matrix: the clusters are preformed in the gas phase using a laser vaporization source working in a low-energy cluster beam deposition (LECBD) system [17]. Deposited in a soft landing regime, the clusters are not fragmented or distorted at the impact on the substrate. Moreover, a quadrupolar electrostatic mass deviator allows us to tighten the size dispersion and to obtain a Gaussian distribution centered at a desired mean value ranging from 2 to 10 nm [18].

The ultrahigh-vacuum chamber (base pressure in the range of 10^{-10} mb) is equipped with an electron-beam evaporator with three targets (Fe, Pt, and Co) that serve to grow films [for matrix, references, and nanofilm (NF) samples] by successive atomic depositions.

To prepare the nanocomposite samples, a first layer of Co clusters is deposited on a Si substrate, then a 1.15-nm film of Fe, then a 1.40-nm third film of Pt from electron-gun evaporation. These three steps are repeated six times in total [see Supplemental Material [19], Fig. S1(a)]. CoFePt nanofilm samples are prepared entirely by electron gun evaporation, with the same atomic Co content as NC samples [Supplemental Material [19], Fig. S1(b)]. Finally, an $L1_0$-FePt NF without Co is prepared as a reference ($L1_0$-FePt ref.). The total thickness of the samples is between 15.3 nm (for $L1_0$-FePt ref.) and 21.3 nm (for 30% Co samples in atomic proportions).

The formation of the magnetically hard $L1_0$ phase is thermally activated upon high-vacuum annealing at 700°C for 20 min [20–22] [Supplemental Material [19], Fig. S1(c)]. The chemical ordering has been observed for annealing temperatures higher than 650°C, with the appearance of the (001) line owing to stacking of pure element planes. The (001)/(110) peak intensity ratio is higher than the one expected for an isotropic polycrystalline system, indicating a partial *c*-axis texture. However, the coexistence of strong (111) and (001) peaks indicates a relatively large angular dispersion in the preferential orientation. Note that similar observations were reported previously in films prepared from alternative deposition of Fe and Pt thin layers [20], where the authors assigned the preferential *c*-axis texture to the growth process.

B. Transmission electron microscopy (TEM) analysis

Bright-field TEM imaging of mass-selected Co clusters protected by a carbon film was performed in a Jeol 2100 HT, operated at 200 kV. Scanning TEM energy-dispersive x-ray (STEM-EDX) experiments were performed in an FEI Titan ETEM G2 60-300, operated at 300 kV. For this purpose, a FePt/Co cluster/FePt specimen was deposited by LECBD directly on the Si_3N_4 membrane of a DENSsolutions Wildfire MEMS chip, maintained at room temperature in the present study.

C. XMCD, XLD, and XANES analyses

Polarization-dependent x-ray absorption, x-ray linear dichroism (XLD), and x-ray magnetic circular dichroism (XMCD) experiments were performed at the ID12 beamline [23] of the European Synchrotron Radiation Facility. The x-ray source for these measurements was the first harmonic of an APPLE-II-type helical undulator (HU-38) in a pure helical mode. The x-ray beam was monochromatized with a fixed-exit double-crystal monochromator equipped with a pair of Si(111) crystals. The x-ray absorption spectra were recorded using the total fluorescence yield detection mode. The x-ray fluorescence signal from the samples was collected in the backscattering geometry, using Si photodiodes. The XLD signal is obtained as the difference between two absorption spectra measured with the x-ray polarization vector being either parallel or nearly perpendicular (80°) to the sample surface. To minimize any eventual experimental artifacts, we kept the sample orientation constant and carried out polarization of x rays using a 0.9-mm-thick diamond quarter-wave plate. The x-ray quarter-wave plate allowed us to transform the incoming circular polarized beam into two orthogonal linearly polarized beams at each energy point of the scan. The absorption was recorded from the same part of the sample for both polarizations. The local magnetic properties of the Fe and Co sites were studied using the XMCD method at the Fe and Co K edge. Measurements were performed at 295 K under an applied magnetic field of 4 T provided by a superconducting solenoid. The angle between the sample surface and the applied field was 10°. The XMCD spectra were obtained as the difference between two consecutive x-ray absorption near-edge-structure (XANES) spectra recorded with opposite photon helicities of the incoming photons. Measurements were performed for both directions of the applied magnetic field, parallel and antiparallel to the incoming x-ray wave vector, in order to ensure the absence of experimental artifacts. The element-selective magnetization curves were recorded by monitoring the intensity of the XMCD signal as a function of an applied magnetic field.

D. EXAFS fitting

The software suite Demeter [24], which includes Athena (data normalization) and Artemis (simulation), was used. This

software allows the fitting of the extended x-ray absorption fine structure (EXAFS) formula signal, allowing, for each atomic shell j around the target atom i, the determination of N_j, the coordination number of atom i; S_i^2, the reduction factor from multielectronic effects; F_j, the backscattering amplitude; σ_j^2, the Debye-Waller factor; $k = \sqrt{\frac{2em_e}{\hbar^2}(E - E_0)}$, the photoelectron wave vector; λ, the mean free path of the photoelectron; r_j, the interatomic distance; and ϕ_{ij}, the phase shift.

After extraction of the EXAFS signal $\chi(k)$ from the absorption signal, its Fourier transform (FT), $\chi(R)$, was restricted to fit the neighboring of the absorbing atom. The fitting is done by modeling the expected spectrum with FEFF6 [25,26], choosing the main paths of the photoelectron, then fitting with more paths as the fitting window is increased to higher radial distances. The S_i^2 parameter, which accounts for the relaxation of the other electrons of the absorbing atom [27], is kept fixed in the fits to a value obtained using pure reference foils of each element: 0.73 for Fe, 0.70 for Co, and 0.84 for Pt. The fitted parameters are the energy edge E_0, allowed to vary slightly according to the sample, the radial distances R_{eff}, to account for distortion of the tested crystal structure R along the a and c axes (while maintaining the cell volume for cubic structures), and the Debye-Waller σ.

The $L1_0$-FePt ref. sample provided a calibration mean for the procedure which led to the best fit with the $L1_0$ structure for this film.

III. RESULTS

The mean size of mass-selected Co clusters is around 7.9 nm in diameter as deposited, as obtained from TEM observation [Figs. 1(a) and 1(b)]. To verify the cluster diameter in the FePt matrix, a single Co cluster layer embedded between two FePt on a Si_3N_4 substrate was prepared to perform energy-dispersive x-ray (EDX) images, provided in Fig. 1(c), where the clusters observed in the metallic matrix have a size compatible with the diameter found by TEM imaging.

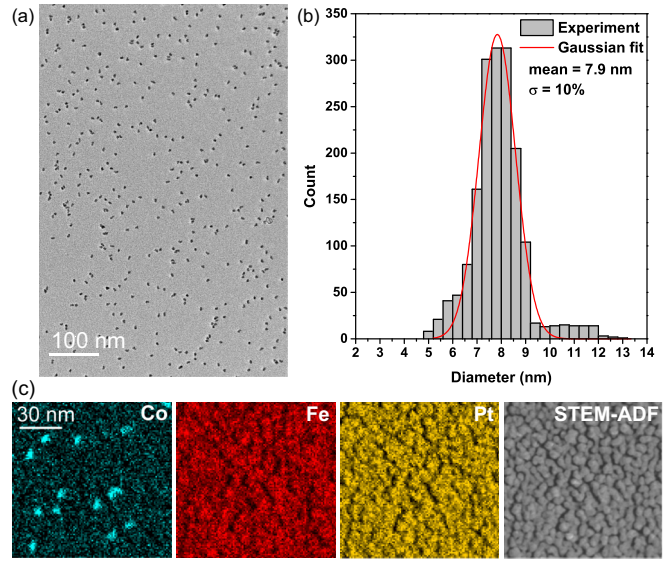

FIG. 1. (a) Bright-field TEM image of mass-selected Co clusters protected by a C film. (b) Size histogram deduced from TEM observations along with the Gaussian fit. (c) EDX images of a FePt/Co cluster/FePt sample on a Si_3N_4 substrate, along with the scanning transmission electron microscopy-annular dark-field (STEM-ADF) image. Both measurements give consistent cluster diameter preannealing, even when embedded in the metallic matrix. The distribution of Fe and Pt is not perfectly homogeneous but reveals "cloudlike" formations, similar to thin-film deposition, which most likely disappear when the thickness increases [28].

A. Magnetic properties

The magnetic properties of Co@FePt nanocomposites were studied by superconducting quantum interference device (SQUID) magnetometry and XMCD experiments performed at room temperature. Figure 2 presents the magnetization curves of an NC and an NF containing 30% Co and an $L1_0$-FePt ref. On the one hand, both the NC and the NF samples have higher saturation magnetization than the $L1_0$-FePt ref., which can be attributed to the higher magnetization of Co compared to FePt. On the other hand, the NC sample exhibits a higher coercivity than the NF, which is magnetically soft as expected for the cubic $L1_2$ phase. The remanence magnetization, measured in plane, is relatively high in all cases (more than 80%) and indicates only partial out-of-plane c texture. Despite the higher magnetization value of the NC, the estimated energy product $(BH)_{max}$ is lower compared to that in the $L1_0$-FePt ref. because of the lower coercive field (Table I).

In the ideal case of a sharp interface between the hard FePt and the soft Co phases, element-specific studies permit the probing of both components separately. The dependence of the XMCD signal as a function of the applied magnetic field (Fig. 3) shows that Fe and Co exhibit the same behavior and switch at the same field value for every concentration

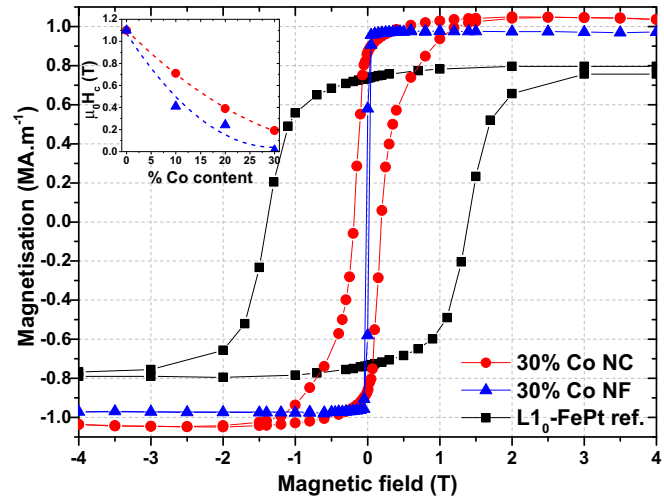

FIG. 2. Hysteresis loops at 300 K for two samples with the same Co content and the FePt matrix without Co. The NC sample has higher saturation magnetization than the bare $L1_0$-FePt ref., which is brought by the Co but retains a sizable coercivity, whereas the NF is magnetically soft. Inset: Dependence of the coercive field $\mu_0 H_c$ on the Co content for the NF and NC (dashed lines are a guide for the eye).

TABLE I. Coercive field and energy product for an NC, an NF, the $L1_0$-FePt ref., and a $Nd_2Fe_{14}B$ random bonded magnet from Coey [4].

	$\mu_0 H_c$ (T)	M_s (MA · m^{-1})	$(BH)_{max}$ (kJ · m^{-3})
30% Co NC	0.18	1.0	63
30% Co NF	0.01	1.0	< 1
$L1_0$-FePt ref.	1.4	0.8	119
$Nd_2Fe_{14}B$	∼0.8	1.3	63

(in the studied range, 0–30% Co), indicating a strong coupling. A slight difference is observed in the coercive field values extracted from XMCD (Fig. 3) and SQUID (Fig. 2) measurements on the same samples. This is attributed to the difference in the probed regions, larger in the case of SQUID measurements.

Isolated face-centered cubic (fcc) Co clusters with a diameter of 7.9 nm are expected to be superparamagnetic at room temperature and, therefore, magnetically soft [29]. Here, there is no kink at low field on the magnetization curve, showing that the whole film behaves like a single magnetic phase and there is no indication of the presence of a secondary magnetic phase. However, it does not give access to the degree of interdiffusion at the cluster-matrix interface, which may lead to different intermixing states [as illustrated in the Supplemental Material [19], Fig. S2). Such an interdiffusion is expected to result in a modulation of the composition with an intermediate diffused layer between a Co core and a FePt matrix that can be denoted (Co@$Co_xFe_yPt_z$@FePt). The ultimate stage of interdiffusion would be a homogeneous alloyed film, which is rather unlikely, as the magnetic properties of the NC differ significantly from those of the reference homogeneous NF.

Apart from the latter hypothesis of a homogeneous configuration, definitely ruled out by SQUID magnetometry measurements, it would be very difficult to discern non-cluster-matrix interdiffusion vs Co@$Co_xFe_yPt_z$@FePt by TEM imaging. X-ray absorption spectroscopy (XAS) studies were thus performed to clarify the local structural properties of the samples.

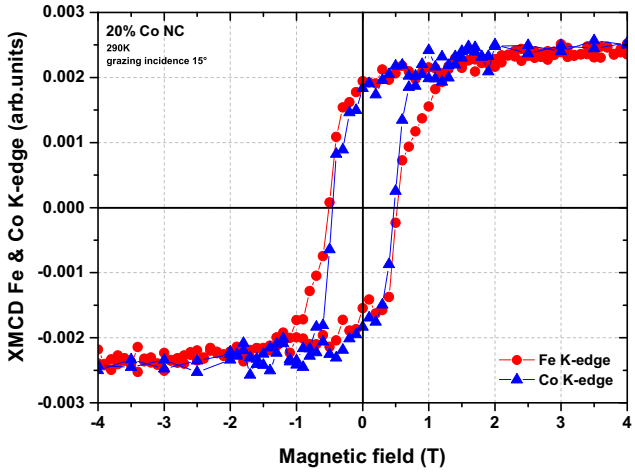

FIG. 3. Hysteresis loops at 290 K of a 20% Co NC sample at the Fe and Co K edges. Both elements show the same coercivity. Note that the deviation of the Fe and Co magnetic moment curves between 0.5 and 1 T is attributed to the lower density of Co clusters at the edge of the probed area in grazing incidence.

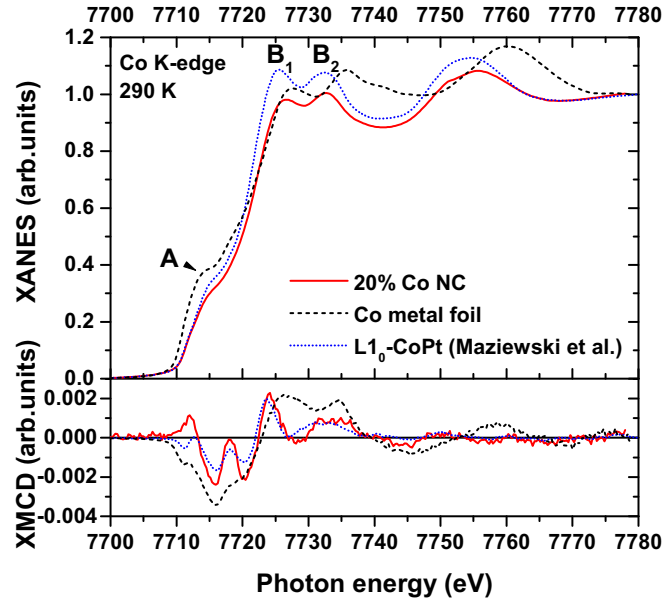

FIG. 4. XANES and XMCD signal at the Co K edge of a 20% Co NC, a Co hcp metallic foil (from a private communication with A. Rogalev and F. Wilhelm), and an $L1_0$-CoPt reference (from Maziewski *et al.* [34]).

B. Structural properties

XANES and XMCD signals at the Co K edge are presented in Fig. 4, for a 20% Co NC sample and Co hexagonal close-packed (hcp) and $L1_0$-CoPt references. The 20% Co NC XANES signal is very different from a Co hcp signal, which shows an important dip in A and a B_2 peak at higher energy [30], whereas the NC sample and references have symmetric B_1 and B_2 features close to one another, characteristic of face-centred tetragonal (as in $L1_0$-FePt and $L1_0$-CoPt) alloyed phases [30,31]. This splitting suggests some alloying of Co with Fe and Pt from the matrix in the NC sample, as expected for the $L1_0$-CoPt reference. Nevertheless, the B_1-B_2 splitting is also present in Co hcp [32,33], and EXAFS measurements were performed to better understand the structure of the NC sample and are detailed later. The XMCD signal of the NC is close to the $L1_0$-CoPt signal, demonstrating that Co is not in a pure metallic state, either hcp or fcc.

XLD measurements at the Fe K edge for 20% Co NC and NF and the $L1_0$-FePt reference (Supplemental Material [19], Fig. S3) reveal significant XLD signal, which proves—at least partial—texturation of the sample, favored by the alternative stacking of the layers [20]. The XANES peaks B_1 and B_2 appear asymmetric only for the NF sample (B_2 feature higher than B_1), which is consistent with a Co enrichment of NF samples, as observed in other studies [35] and the XANES of the hcp Co. The shoulder A, mainly due to Co and Fe $4p$ orbitals [31], is larger for the NF, as expected for a more complete mixing in the NF compared to the NC.

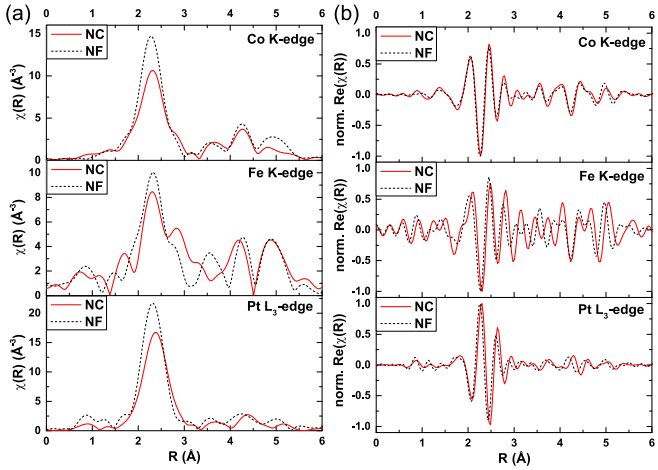

FIG. 5. Comparison of (a) the magnitude and (b) the real part of the FT of the EXAFS signal for a 30% Co NC and a 30% Co NF at each edge.

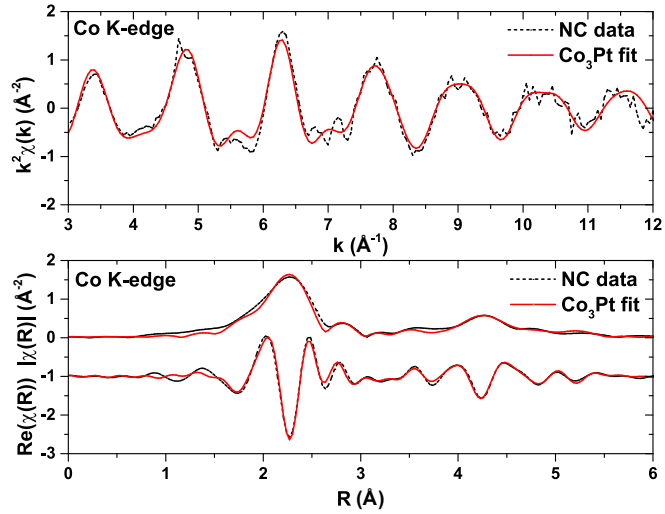

FIG. 6. Weighted EXAFS oscillations, magnitude of the filtered signal, and real part of the FT of the 30% Co NC sample at the Co K edge, along with the Co_3Pt fit.

To study the local structure of the samples, XAS measurements were performed to obtain the specific EXAFS signature at the Fe and Co K edges and Pt L_3 edge (see Supplementary Material [19] methods for details [24,27]). Figure 5 presents the modulus and real part of the FT of the EXAFS signal for the 30% Co NC and NF, giving an additional qualitative indication of different local environments in both systems. The comparison to the $L1_0$-FePt ref. (Supplemental Material [19], Fig. S4) shows that the NC is much closer to this phase at the Fe K edge. This is an argument in favor of a stronger Co-matrix diffusion in the NF than in the NC, which could also explain the low coercivity obtained for this NF sample. As Co and Fe show similar binary phase diagrams with Pt [36], the more atomic interdiffusion occurs, the more the stable phase shifts towards higher Co + Fe content values, leading to a magnetically soft $L1_2$-X_3Pt (with $X = \mathrm{Co, Fe}$) when the Co content is high enough (as in 30% Co samples).

Two kinds of simulation have been realized to analyze the spectra: the first fit is performed on a wide radial distance (typically between 1.5 and 5.5 Å) at each edge, with different possible crystal alloy phases, by setting the nature and number of neighboring atoms N_j. The best fits from this method for each edge are listed in Table II (detailed EXAFS results are provided in the Supplementary Material tables [19]).

For the 30% NC sample, the EXAFS simulations at the Fe K edge and Pt L_3 edge lead to an $L1_0$-FePt structure. On the contrary, for the NF sample, the optimized structure is a mixed X_3Pt structure at the Fe K edge and Pt L_3 edge, confirming strong Co-matrix intermixing in this sample. Distinguishing Fe from Co neighboring atoms based on EXAFS measurements is a difficult task (as $\Delta Z = 1$). Nevertheless, the fact that the Co_3Pt phase fits only at the Co K edge in the NC samples (Fig. 6), while the $L1_0$-FePt phase fits at the Fe K and Pt L_3 edges, suggests the persistence of Co-rich regions.

TABLE II. Structure giving the best fits for a window between 1.5 and 5.5 Å ($X = \mathrm{Co, Fe}$).

Best fit at	NC	NF
Co K edge	X_3Pt	X_3Pt
Fe K edge	$L1_0$-FePt	X_3Pt
Pt L_3 edge	$L1_0$-FePt	X_3Pt

To quantify atomic interdiffusion between cluster and matrix in the NC, another fit is performed at the Co K edge on NC samples, by choosing small radial distances (between 1.5 and 3.0 Å) that limit us to the first neighbors of the Co atoms. The fit is realized with Co (accounting for both Co and Fe atoms) and Pt atoms, initially at positions found from the previous Co_3Pt fit. The coordination numbers N_j are then set free (but limited to $N_{\mathrm{Co,Fe}} + N_{\mathrm{Pt}} = 12$) and have been obtained by the fit at different angles. The number of Co-Co bonds is found to be on average centered on $N_{\mathrm{Co\text{-}Co}} = 4.2$ (Supplemental Material [19], Fig. S5).

In addition, a diffusion of the cluster is simulated from an initial truncated-octahedron Co cluster (stable shape of fcc clusters [37]) of 11 atoms per ridge (which corresponds to the size observed by TEM) inserted in an FePt matrix. A simple iterative diffusion algorithm is then applied to every atom by setting a 50% probability of swapping its place with a neighboring atom. The mean number of Co-Co bonds is then calculated and compared to the number obtained by EXAFS fitting. These steps are repeated until the coordination number of the model is equal to or lower than that obtained from the EXAFS. It results that this 4.2 coordination number can occur when matrix atoms reach the center of the cluster (Supplemental Material [19], Fig. S6), but the Co concentration remains above 75% in a radius of at least 1.8 nm.

For NCs, the important criterion is the core size of the soft inclusion. According to the Co-Pt (or Fe-Pt) phase diagrams, the edge of the $L1_0$ phase is at least 35% content in Co (or Fe) [36]. Therefore, with Co-content clusters embedded in a hard $L1_0$ matrix, the soft inclusion of X_3Pt remains around 7.4 nm in diameter after annealing (Supplemental Material [19], Fig. S7).

IV. CONCLUSION

Magnetic measurements of the composition dependence of the coercive field as well as EXAFS fitting and simulation treatment prove that, after annealing at 700°C for 20 min, NCs still present high-Co-content inclusions well coupled to the matrix, contrary to NFs, where the interdiffusion is complete. To explain this result, first, one can mention that clusters have a well-defined shape as prepared and are particularly stable [38]. Second, for the same amount of Co in a sample, the thickness of the Co layer in an NF (1.0 nm for 30% Co) is smaller than the radius of a cluster as prepared, favoring total Co-atomic diffusion in the matrix during annealing. This lower diffusion in NCs allows the matrix to stay in the $L1_0$ stability domain, maintaining the magnetic hardness of the sample.

Moreover, the cluster diffusion simulation does not take into account the different miscibility as well as the different sizes of Fe, Co, and Pt atoms, which can lead to different diffusion coefficients [36]. As such, heavy Pt atoms in the matrix are less likely to diffuse into the Co cluster. Crystal distortions of the fcc Co-rich regions in the face-centered tetragonal (fct) $L1_0$ matrix have also been neglected in the simulation but are revealed by the EXAFS fitting.

One of the key factors to improve the $(BH)_{max}$ is better control of the cluster-matrix interdiffusion: with thinner layers of Fe and Pt and a larger number of repetitions, annealing to form the $L1_0$ phase can be achieved at a lower temperature and more rapidly. Moreover, the maximum of coercivity for nonepitaxial thin films is not reached for $Fe_{50}Pt_{50}$ but, rather, for $Fe_{53}Pt_{47}$ [22,39]. Although pure Co clusters provide the opportunity to visualize soft and hard phases individually, they do not support a high $(BH)_{max}$, as the highest moment per atom is reached for $Fe_{65}Co_{35}$ [5]. Finally, the texturation of the hard magnetic matrix could be improved using a MgO crystal substrate. These Co@FePt samples are a proof of concept of NC permanent magnets, stabilizing the moments of the soft clusters at room temperature.

ACKNOWLEDGMENTS

The authors thank Florent Tournus (iLM laboratory) for his help on the cluster modeling, Nicholas Blanchard (iLM laboratory) for TEM imaging, and José Penuelas (STMS/INL) for XRD measurements. STEM-EDX experiments were performed at the Consortium Lyon St. Etienne de Microscopie. XMCD, XLD, XANES, and EXAFS measurements were made at the European Synchrotron Radiation Facility, on beamline ID12 and on French CRG BM30B FAME for the latter. This work was supported by the Agence Nationale de la Recherche (ANR) through the collaborative project SHAMAN (ANR-16-CE09-0019) and the doctoral school ED PHAST 52. The authors are also grateful to the ILMTECH platform for cluster synthesis at PLYRA and SQUID measurements at the Centre de Magnétométrie de Lyon.

[1] T. N. A. Nguyen, Y. Fang, V. Fallahi, N. Benatmane, S. M. Mohseni, R. K. Dumas, and J. Åkerman, [Co/Pd]-NiFe exchange springs with tunable magnetization tilt angle, Appl. Phys. Lett. **98**, 172502 (2011).

[2] D. Mitin, M. Wachs, N. Safonova, O. Klein, and M. Albrecht, Exchange coupled L10 FeCuPt/Fe heterostructures: Magnetic properties and reversal behavior at elevated temperatures, Thin Solid Films **651**, 158 (2018).

[3] B. Ma, G. Y. Situ, H. G. Chu, and J. P. Wang, Exchange coupled composite FePt/TbCo/[Co/Ni]N films with a TbCo interlayer, AIP Adv. **7**, 056508 (2017).

[4] J. Coey, Perspective and prospects for rare earth permanent magnets, Engineering **6**, 119 (2020).

[5] J. M. D. Coey, *Magnetism and Magnetic Materials*, 1st ed. (Cambridge University Press, Cambridge, UK, 2001).

[6] T. Burkert, L. Nordström, O. Eriksson, and O. Heinonen, Giant Magnetic Anisotropy in Tetragonal FeCo Alloys, Phys. Rev. Lett. **93**, 027203 (2004).

[7] X. Li, L. Lou, W. Song, G. Huang, F. Hou, Q. Zhang, H.-T. Zhang, J. Xiao, B. Wen, and X. Zhang, Novel bimorphological anisotropic bulk nanocomposite materials with high energy products, Adv. Mater. **29**, 1606430 (2017).

[8] J. Lucas, P. Lucas, T. Le Mercier, A. Rollat, and W. Davenport, *Rare Earths: Science, Technology, Production and Use* (Elsevier, Amsterdam, 2015).

[9] P. Mcguiness, O. Akdogan, A. Asali, S. Bance, F. Bittner, J. M. D. Coey, N. M. Dempsey, J. Fidler, D. Givord, O. Gutfleisch *et al.*, Replacement and original magnet engineering options (ROMEOs): A European Seventh Framework project to develop advanced permanent magnets without, or with reduced use of, critical raw materials, J. Operat. Manage. **67**, 1306 (2015).

[10] J. Rial, P. Švec, E. Palmero, J. Camarero, P. Švec, and A. Bollero, Severe tuning of permanent magnet properties in gas-atomized MnAl powder by controlled nanostructuring and phase transformation, Acta Mater. **157**, 42 (2018).

[11] E. Kneller and R. Hawig, The exchange-spring magnet: A new material principle for permanent magnets, IEEE Trans. Magn. **27**, 3588 (1991).

[12] R. Coehoorn, D. De Mooij, and C. De Waard, Meltspun permanent magnet materials containing Fe_3B as the main phase, J. Magnet. Magnet. Mater **80**, 101 (1989).

[13] R. Skomski and J. M. D. Coey, Giant energy product in nanostructured two-phase magnets, Phys. Rev. B **48**, 15812 (1993).

[14] R. Skomski, P. Manchanda, P. K. Kumar, B. Balamurugan, A. Kashyap, and D. J. Sellmyer, Predicting the future of permanent-magnet materials, IEEE Trans. Magn. **49**, 3215 (2013).

[15] X. Rui, J. Shield, Z. Sun, L. Yue, Y. Xu, D. Sellmyer, Z. Liu, and D. Miller, High-energy product exchange-spring FePt/Fe cluster nanocomposite permanent magnets, J. Magn. Magn. Mater. **305**, 76 (2006).

[16] M. Yue, X. Zhang, and J. P. Liu, Fabrication of bulk nanostructured permanent magnets with high energy density: Challenges and approaches, Nanoscale **9**, 3674 (2017).

[17] V. Dupuis, G. Khadra, A. Hillion, A. Tamion, J. Tuaillon-Combes, L. Bardotti, and F. Tournus, Intrinsic magnetic

properties of bimetallic nanoparticles elaborated by cluster beam deposition, Phys. Chem. Chem. Phys. **17**, 27996 (2015).

[18] R. Alayan, L. Arnaud, A. Bourgey, M. Broyer, E. Cottancin, J. R. Huntzinger, J. Lermé, J. L. Vialle, M. Pellarin, and G. Guiraud, Application of a static quadrupole deviator to the deposition of size-selected cluster ions from a laser vaporization source, Rev. Sci. Instrum. **75**, 2461 (2004).

[19] See Supplemental Material at http://link.aps.org/supplemental/10.1103/PhysRevB.102.224409 for additional figures and tables.

[20] H. Zeng, M. L. Yan, N. Powers, and D. J. Sellmyer, Orientation-controlled nonepitaxial l10 CoPt and FePt films, Appl. Phys. Lett. **80**, 2350 (2002).

[21] Y. Liu, T. A. George, R. Skomski, and D. J. Sellmyer, Aligned and exchange-coupled l10 (Fe,Co)Pt-based magnetic films, J. Appl. Phys. **111**, 07B537 (2012).

[22] M. H. Hong, K. Hono, and M. Watanabe, Microstructure of FePt/Pt magneticthin films with high perpendicular coercivity, J. Appl. Phys. **84**, 4403 (1998).

[23] A. Rogalev and F. Wilhelm, Magnetic circular dichroism in the hard x-ray range, Phys. Met. Metallogr. **116**, 1285 (2015).

[24] B. Ravel and M. Newville, Athena, Artemis, Hephaestus: Data analysis for x-ray absorption spectroscopy using IFEFFIT, J. Synchrotron Radiat. **12**, 537 (2005).

[25] J. J. Rehr and R. C. Albers, Theoretical approaches to x-ray absorption fine structure, Rev. Mod. Phys. **72**, 621 (2000).

[26] J. J. Rehr, J. J. Kas, M. P. Prange, A. P. Sorini, Y. Takimoto, and F. Vila, Ab initio theory and calculations of x-ray spectra, C. R. Phys. **10**, 548 (2009).

[27] B. K. Teo, *EXAFS: Basic Principles and Data Analysis* (Springer, Berlin, 2014).

[28] A. I. Figueroa, J. Bartolomé, L. M. García, F. Bartolomé, O. Bunău, J. Stankiewicz, L. Ruiz, J. M. González-Calbet, F. Petroff, C. Deranlot and S. Pascarelli, P. Bencok, N. B. Brookes, F. Wilhelm, A. Smekhova, and A. Rogalev, Structural and magnetic properties of granular Co-Pt multilayers with perpendicular magnetic anisotropy, Phys. Rev. B **90**, 174421 (2014).

[29] M. Jamet, W. Wernsdorfer, C. Thirion, D. Mailly, V. Dupuis, P. Mélinon, and A. Pérez, Magnetic Anisotropy of a Single Cobalt Nanocluster, Phys. Rev. Lett. **86**, 4676 (2001).

[30] J.-I. Park, M. G. Kim, Y.-w. Jun, J. S. Lee, W.-r. Lee, and J. Cheon, Characterization of superparamagnetic core-shell nanoparticles and monitoring their anisotropic phase transition to ferromagnetic solid solution nanoalloys, J. Am. Chem. Soc. **126**, 9072 (2004).

[31] N. M. Souza-Neto, A. Y. Ramos, H. C. N. Tolentino, and Y. Joly, Depth dependent local structures in CoPt thin films, J. Phys.: Conf. Ser. **190**, 012112 (2009).

[32] Y. A. Kozinkin, A. A. Novakovich, A. V. Kozinkin, R. V. Vedrinskii, Y. V. Zubavichus, and A. A. Veligzhanin, Mechanisms of formation of near-edge fine structure of K x-ray absorption spectra of metallic Cu, Ni, Co (hcp and fcc phases), and Cr, Phys. Solid State **53**, 1 (2011).

[33] P. Mazalski, I. Sveklo, Z. Kurant, K. Ollefs, A. Rogalev, F. Wilhelm, J. Fassbender, L. T. Baczewski, A. Wawro, and A. Maziewski, XAS and XmCd studies of magnetic properties modifications of Pt/Co/Au and Pt/Co/Pt trilayers induced by Ga^+ ions irradiation, J. Synchrotron Radiat. **22**, 753 (2015).

[34] A. Maziewski, P. Mazalski, Z. Kurant, M. O. Liedke, J. McCord, J. Fassbender, J. Ferré, A. Mougin, A. Wawro, L. T. Baczewski, A. Rogalev, F. Wilhelm, and T. Gemming, Tailoring of magnetism in Pt/Co/Pt ultrathin films by ion irradiation, Phys. Rev. B **85**, 054427 (2012).

[35] E. K. Hlil, R. Baudoing-Savois, B. Moraweck, and A. J. Renouprez, X-ray absorption edges in platinum-based alloys. 2. Influence of ordering and of the nature of the second metal, J. Phys. Chem. **100**, 3102 (1996).

[36] C. J. Smithells, W. F. Gale, and T. C. Totemeier, *Smithells Metals Reference Book*, 8th ed. (Elsevier Butterworth-Heinemann, Amsterdam, 2004).

[37] R. Van Hardeveld and F. Hartog, The statistics of surface atoms and surface sites on metal crystals, Surf. Sci. **15**, 189 (1969).

[38] R. Ferrando, *Structure and Properties of Nanoalloys. Frontiers of Nanoscience* (Elsevier, Amsterdam, 2016).

[39] M. Watanabe and M. Homma, Perpendicular magnetization of epitaxial FePt(001) thin films with high squareness and high coercive force, Jpn. J. Appl. Phys. **35**, L1264 (1996).